ELSEVIER

Journal of Fluids and Structures 22 (2006) 401–419

JOURNAL OF FLUIDS AND STRUCTURES

www.elsevier.com/locate/jfs

Effect of flexure on aerodynamic propulsive efficiency of flapping flexible airfoil

J.-M. Miao[a,*], M.-H. Ho[b]

[a]*Department of Mechanical Engineering, Chung Cheng Institute of Technology, National Defense University, Taiwan 355, ROC*
[b]*Graduate School of Defense Science Studies, Chung Cheng Institute of Technology, National Defense University, Taiwan 355, ROC*

Received 15 March 2005; accepted 21 November 2005
Available online 25 January 2006

Abstract

The aim of present study is to investigate the effect of chord-wise flexure amplitude on unsteady aerodynamic characteristics for a flapping airfoil with various combinations of Reynolds number and reduced frequency. Unsteady, viscous flows over a single flexible airfoil in plunge motion are computed using conformal hybrid meshes. The dynamic mesh technique is applied to illustrate the deformation modes of the flexible flapping airfoil. In order to investigate the influence of the flexure amplitude on the aerodynamic performance of the flapping airfoil, the present study considers eight different flexure amplitudes (a_0) ranging from 0 to 0.7 in intervals of 0.1 under conditions of $\mathrm{Re} = 10^4$, reduced frequency $k = 2$, and dimensionless plunge amplitude $h_0 = 0.4$. The computed unsteady flow fields clearly reveal the formation and evolution of a pair of leading edge vortices along the body of the flexible airfoil as it undergoes plunge motion. Thrust-indicative wake structures are generated when the flexure amplitude of the airfoil is less than 0.5 of the chord length. An enhancement in the propulsive efficiency is observed for a flapping airfoil with flexure amplitude of 0.3 of the chord length. This study also calculates the propulsive efficiency and thrust under various Reynolds numbers and reduced frequency conditions. The results indicate that the propulsive efficiency has a strong correlation with the reduced frequency. It is found that the flow conditions which yield the highest propulsive efficiency correspond to Strouhal number St of 0.255.

1. Introduction

The effective flight capabilities of birds and insects have long fascinated biological scientists and researchers involved in the investigation of low Reynolds number aerodynamic regimes. The ability of winged birds and insects to hover, take off, and land etc. via flapping propulsion has inspired researchers and aviation engineers to consider equipping aircraft with flapping mechanisms rather than rotating mechanisms as a means of generating thrust and lift forces. Many examples can be found in nature of winged creatures exhibiting excellent aerodynamic characteristics. In many cases, the capabilities of these creatures exceed those demonstrated by man-made aircraft. The application of flapping wings in wind and water energy conversion plants has been actively considered in recent years. Moreover, a significant development anticipated in the aviation field is the production of an increasing number of civilian and military micro-aviation-vehicles (MAV) applications over the coming decade.

*Corresponding author. Fax: +886 03 3895924.
E-mail address: jmmiao@ccit.edu.tw (J.-M. Miao).

0889-9746/$ - see front matter © 2005 Elsevier Ltd. All rights reserved.
doi:10.1016/j.jfluidstructs.2005.11.004

Nonmenclature

a_0	flexure amplitude of airfoil
C	chord-wise length of airfoil
C_d	drag coefficient
C_l	lift coefficient
dS_n/dt	velocity normal to the surface of airfoil
f	flapping frequency
$\bar{F}_x$	period-averaged thrust force
F_x	x-direction force on the surface of airfoil
F_n	force normal to the surface of airfoil
h_0	nondimensional plunge amplitude
h	instantaneous plunge position
k	reduced frequency, $\omega c/U_\infty$
Re	Reynolds number, $\rho U_\infty\ c/\mu$
$\bar{P}$	period-averaged consumption power rate
St	Strouhal number, $2h_0f/U_\infty$
t	dimensional time
t'	nondimensional time, tU_∞/c
T	flapping period, $2\pi/\omega$
U_∞	free-stream velocity
x,y	Cartesian coordinate axis
δ	period-averaged input power coefficient
η	propulsive efficiency, ξ/δ
ξ	period-averaged thrust power coefficient
ρ	density of fluid
Ψ	phase angle between plunging and flexing of airfoil
Ω	circular frequency of flapping oscillations, $2\pi f$

The term "MAV" has been defined by the Defense Air-Borne Reconnaissance Office (DARO) as a miniature remote-controlled aircraft with a wingspan of 6 in (15 cm) or less and a flight speed of 30–60 km/h (i.e. 8.33–16.67 m/s). Some MAV designs use propellers as the propulsive system to generate the necessary thrust. In this mode, the passage of the airstream over the vehicle's fixed rigid wings generates lift as a result of the pressure difference generated between the upper and lower wing surfaces. The MicroSTAR MAV is a typical example of this type of approach. However, flapping-wing propulsion systems not only enhance the flight efficiency of a MAV, but also equip it with the ability to perform delicate maneuvers in extreme situations. From a low-Reynolds-number aerodynamics perspective, flapping-wing propulsion systems are more efficient than their conventional rotational propeller counterparts (Tuncer and Kaya, 2003). Murray and Howle (2003) conducted their research with a flexible oscillating thin airfoil and found that the flexible airfoils may produce larger aerodynamic efficiency than rigid airfoils. Moreover, the requirements of military planners for an MAV capable of hovering and maneuvering stably in confined spaces in order to perform a remote reconnaissance role, while also having the ability to take off and land on a variety of terrains, are driving researchers to investigate efficient flapping-wing propulsive technologies. Rozhdestvensky and Ryzhov (2003) published a comprehensive survey of the research and development results for flapping-wing propulsors. Fig. 1 presents a photograph of the flapping-wing propelled, radio-controlled MAV developed by Jones et al. (2004).

The first recorded researchers to observe the unsteady flow dynamic characteristics of a flapping wing were Knoller (1909) and Betz (1912). According to the Knoller–Betz effect, an insect has the ability to generate a propulsive force by establishing a sinusoidal angle of attack of the airfoil during rapid flapping motion. The major flow-field characteristic associated with an oscillating airfoil is a pair of asymmetric regular leading vortices located above and below the airfoil. As the airfoil plunges cyclically through the down-stroke and up-stroke stages, the traveling leading edge vortices are shed from the trailing edge and form wake vortices. In the early 1940s, von Kármán and Burgers (1943) provided a theoretical explanation for the different patterns observed for large-scale drag-indicative wake vortices and thrust-indicative wake vortices. The authors reported that the pattern of drag-indicative wake vortices is analogous to the von Kármán vortex street observed behind a bluff body, while that of thrust-indicative wake vortices is similar to jet flow.

Reflecting the rapid growth of interest in biomimetic propulsion, the published literature now contains many experimental and computational investigations of the propulsive characteristics of flapping airfoils. In general, these studies aim to evaluate the effect of the amplitude and frequency of the flapping motion on the generated propulsive efficiency and thrust for various shapes of airfoil. Lai and Platzer (2001) and Jones et al. (1998) used a flow visualization method to illustrate the wake vortex patterns under different reduced frequencies for an oscillating NACA 0012 airfoil. Meanwhile, Anderson (1998) observed that the phase angle between the pitch and the plunge of an oscillating airfoil plays a significant role in maximizing the propulsive efficiency. Read et al. (2003) performed systematic tests to investigate the effects of the heave amplitude, Strouhal number, angle of attack, and phase angle between the heave and the pitch on the propulsive and maneuvering behaviors of an oscillating NACA 0012 airfoil under harmonic motion. Their results indicated that the oscillating airfoil was capable of delivering a satisfactory thrust performance, provided that an appropriate combination of the aforementioned parameters was specified. In a recent study, Hover et al. (2004) developed a novel method for precisely controlling the profile of the airfoil's angle of attack rather than simply adopting a harmonic profile. It was shown that a significant increase in the thrust and efficiency could be achieved by explicitly controlling the angle of the attack profile. Of the four angle of attack profiles considered, it was found that the cosine

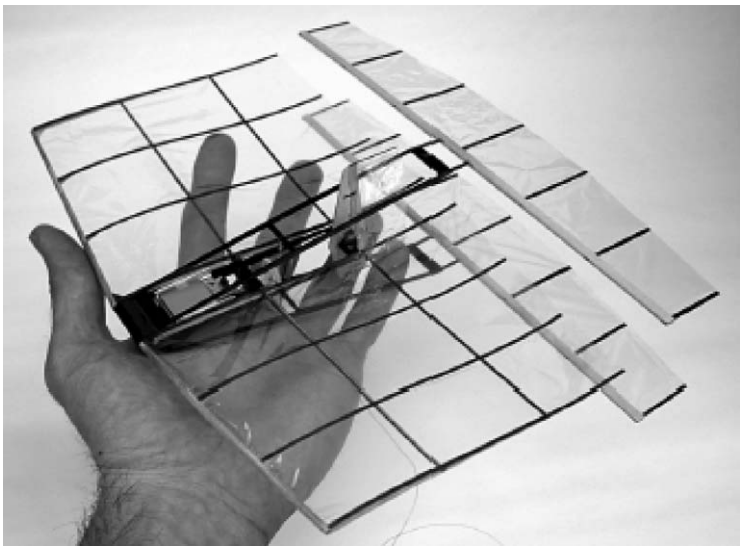

Fig. 1. NPS flapping-wing MAV model developed by Jones et al. (2004).

profile yielded the most significant improvement in efficiency, since in this case only two large vortices were formed and shed at the trailing edge of the airfoil. However, the highest thrust coefficient was obtained when the prescribed motion of the airfoil was performed with a sawtooth angle of attack profile. Heathcote et al. (2004, 2005) developed a new chord-wise flexible airfoil model and tested the effect of airfoil stiffness on propulsive efficiency at zero free-stream velocity and at low Reynolds numbers. The outcome showed that thrust/input-power ratio benefited from the chord-wise flexible airfoil as compared with that for the rigid airfoil.

Tuncer and Platzer (1996) explored the unsteady flow fields and mechanisms of thrust generation for airfoils flapping in a pitching mode by solving the Navier–Stokes equation using an inertial frame of reference. In their study, the flapping motion was implemented by moving the airfoil and the surrounding computational grid in the transverse direction. The results indicated that specifying a flapping amplitude of 0.4 of the chord length and a reduced frequency of 0.1 enhanced the propulsive efficiency of a single NACA 0012 airfoil by up to 70%. Isogai et al. (1999) simulated the more complex unsteady flow field induced by the coupled pitching and heaving oscillations of a single airfoil under various combinations of phase difference and reduced frequency. Their study focused specifically on the dynamic stall behavior of the airfoil and reported that the occurrence of large-scale leading-edge separation degraded the propulsive efficiency. Tuncer and Kaya (2003) predicted the unsteady aerodynamic characteristics of flapping wings in a biplane configuration by solving the viscous Navier–Stokes equations using moving overset grids. The thrust enhancement identified for flapping wings in a biplane configuration was attributed to the suppression of large-scale leading and trailing edge vortices by a combined pitch and plunge motion separated by an appropriate phase shift.

The published literature contains only a few studies into the unsteady aerodynamic behavior of a single flexible airfoil executing flapping motion. Consequently, the present study computes the unsteady viscous flows over a flapping NACA0014 airfoil with various values of flexure amplitude a_0 (see Fig. 3) by solving the Navier–Stokes equations using conformal-hybrid grids. The dynamic mesh technique is adopted to demonstrate the effect of the flexure amplitude on the unsteady aerodynamic characteristics of the flapping airfoil as it undergoes cyclic plunge motion. The influence of the flexure amplitude of the airfoil on the generated thrust and propulsive efficiency are established and discussed.

2. Numerical methodology

2.1. Navier–Stokes solver

This study computes the unsteady viscous flow-fields by solving the Navier–Stokes equations using conformal-hybrid grids. The simulations are performed using the commercial code Fluent 6.1 based on the control-volume method. The flow field in all runs is assumed to be laminar, and the conservative variables are solved sequentially.

The convective flux and diffusive flux terms are evaluated using the third-order accurate QUICK scheme and the second-order accurate central difference scheme, respectively. Meanwhile, the coupling between the pressure and the velocity is achieved by means of the PISO algorithm. The time accuracy is improved by utilizing the FAS multi-grid method. The residual smoothing approach is also applied to accelerate the convergence in solutions within each physical time step. The dynamic mesh technique is employed to model the flapping motion of airfoils with various flexure amplitudes. In each time interval, the temporal grid deformation is governed by the Geometric Conservation Law (GCL).

2.2. Computational grids and boundary conditions

The selection of an appropriate grid generation topology for the aerodynamic prediction of flapping wings is an essential part of the CFD process. Tuncer and Kaya (2003) used overset grids to obtain reasonable solutions for a single rigid flapping airfoil. However, the dynamic mesh technique represents a viable alternative for simulating the unsteady flow field induced by a flapping airfoil with various modes. Fewer restrictions exist on the implementation of the dynamic mesh technique in a computational domain filled with triangular cells. In order to simulate precisely the developing boundary layer flow on the flapping airfoil, the current study adopts the conformal hybrid mesh system. This strategy is based on earlier observations of Isogai et al. (1999) and Tuncer and Kaya (2003), who suggested that the aerodynamic loads of a flapping airfoil are dominated by the formation of leading edge vortices and the subsequent shedding of wake vortices from the trailing edge. It is well known that quadrilateral cells can capture the boundary layer more precisely than triangular cells.

Fig. 2 illustrates the conformal hybrid mesh system employed for the single flexible airfoil under consideration. Following grid refinement studies, the final computational domain is composed of 5356 inner quadrilateral cells and 25 764 outer triangular cells. The C-type quadrilateral cells are used to encompass the entire airfoil and the dynamic stretch and compression mesh method is applied to model the temporal grid deformations during plunge motion for airfoils with various flexure amplitudes. The distributions of the outer triangular cells are reconstructed according to the relative position of the flapping airfoil. The interface between the quadrilateral cells and the triangular cells is modeled by conformal type cells to ensure the conservation of flux for all variables. Both the inner quadrilateral cells and the outer triangular cells are regenerated at each time step.

The present study simulates a single NACA0014 airfoil with different flexure amplitude deformations as it executes plunge motion. The plunge motion of the airfoil shown in Fig. 3 is expressed by

$$h = h_0 c \cos(\omega t), \tag{1}$$

where h denotes the instantaneous position of the airfoil, h_0 denotes dimensionless stroke amplitude, c denotes the chord length of the airfoil, and ω denotes the flapping frequency.

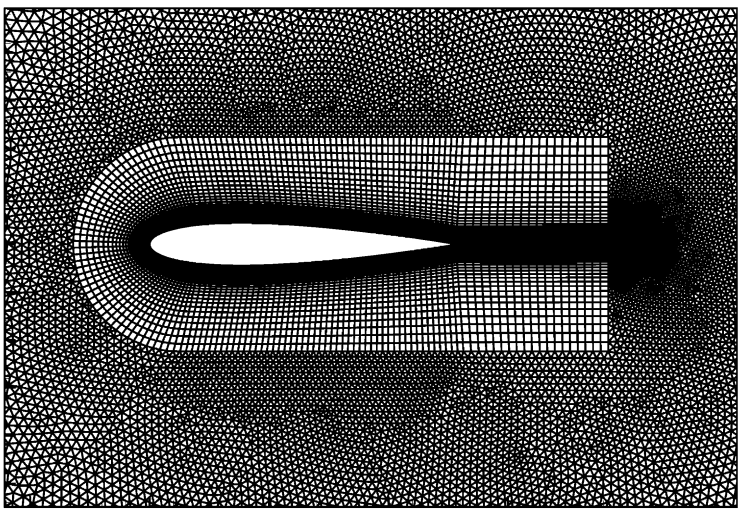

Fig. 2. Conformal hybrid mesh system for single flexible airfoil.

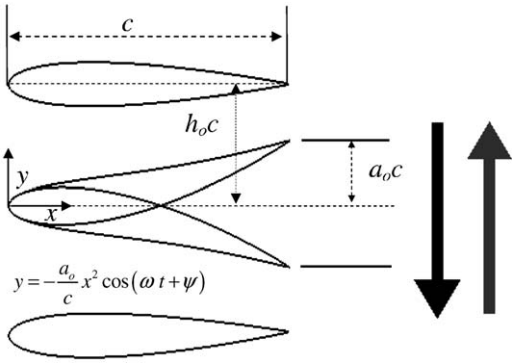

Fig. 3. Plunge and deflection motion of single flexible airfoil. (Black: down stroke stage; Red: up stroke stage, phase angle $\psi = 90^o$).

The inspiration for the present type of deformation comes from the hydrodynamics of fishlike swimming. According to the principles of creature locomotion (Alexander, 1982), the fish can produce great propulsive force by means of body wiggle; but the influence of airfoil flexibility remains unclear in insect flight (Maxworthy, 1981). Sitti et al. (2001) have developed the active flexible flapping plate by using PZT and PZN-PT based unimorph to actuate the flexure motion of the flat plate. The airfoil deformation of a flying creature is not easy to describe precisely. In this work, a simplification on the deformation of the airfoil has been done and facilitated the analysis of the effect of flexure amplitude. Therefore, we assumed that the profile of the flexible airfoil varies over time and is calculated as follows:

$$y = -\frac{a_0}{c}x^2\cos(\omega t + \psi), \tag{2}$$

where a_0 denotes the flexure amplitude(see Fig. 3) and ψ denotes the phase angle. It should be noted that the x–y local frame expressed in the above equation refers to the body coordinate system.

The instantaneous flow velocity in the computing domain must be equal to the local surface velocity described by the plunge and flexure motion of the flapping wing. A no-slip boundary condition is imposed on the airfoil surfaces. Meanwhile, inflow and outflow boundary conditions are imposed on the outer boundary faces, as shown in Fig. 2. Free-stream velocity and zero static pressure conditions are specified at the inflow boundary and outflow boundary, respectively. The reference pressure is taken as 1 atm throughout the current simulation runs. In general, it is found that a periodic solution is obtained after four to six cycles of time iterations. The solution is considered to have converged satisfactorily when the difference between the thrust coefficient and propulsive efficiency values generated in successive cycles of iterations is less than 0.1%.

3. Grid sensitivity test and code validation

In order to test the grid sensitivity, the unsteady flow fields of a rigid airfoil were computed under conditions of $k = 2$, $h_0 = 0.4$, $M = 0.1$ and $\mathrm{Re} = 10^4$ with four different grid system distributions. The total number of quadrilateral and triangular cell numbers and the first layer cell spacing above the airfoil surfaces for each grid system are summarized in Table 1. Fig. 4 provides close-up views of the four grid distributions around the leading edge of the airfoil. Note that the grid size of Mesh A is approximately twice that of Mesh B in both the streamwise and normal directions of the airfoil surfaces. Similarly, the grid size of Mesh B is twice that of Mesh C, etc.

Fig. 5 presents the variation in the calculated coefficient drag, C_d, with respect to nondimensional time ($t' = tU_\infty/c$) for each of the four grid systems. It is evident that, compared to the other meshes, Mesh A yields a marked underestimation of the thrust. Mesh B provides a demonstrable improvement in the thrust estimation. However, this study adopted Mesh C for the remaining simulation runs since it is computationally less intensive than Mesh D, but provides virtually identical results.

In order to validate the present conformal hybrid grid system and computational code, this study computed the time variation of the flapping airfoil position and the corresponding C_d value, and compared the results with those obtained by Tuncer and Kaya (2003). Note that the two studies solved the unsteady, viscous flow field using different grid systems, i.e. Tuncer et al. constructed the computational domain using overset grids, while the present study utilized conformal hybrid grids. However, as shown in Fig. 6, the variations over time of the drag coefficients obtained from the two studies are in reasonably good agreement.

Table 1
Grid refinement test

Model	Quadrilateral cell numbers	Triangle cell numbers	Near wall cell height
Mesh A	315	1729	0.010×64 mm
Mesh B	1260	6640	0.005×64 mm
Mesh C	5363	25 763	0.002×64 mm
Mesh D	22 125	92 549	0.001×64 mm

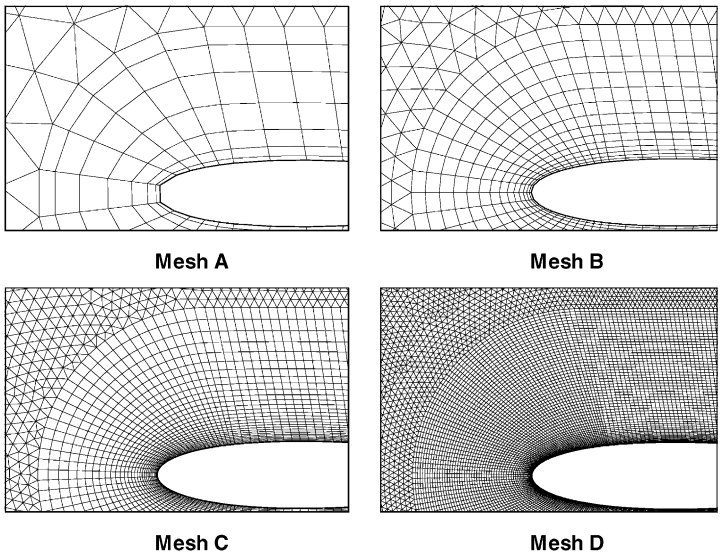

Fig. 4. Close-up views of four tested grids around leading edge of airfoil.

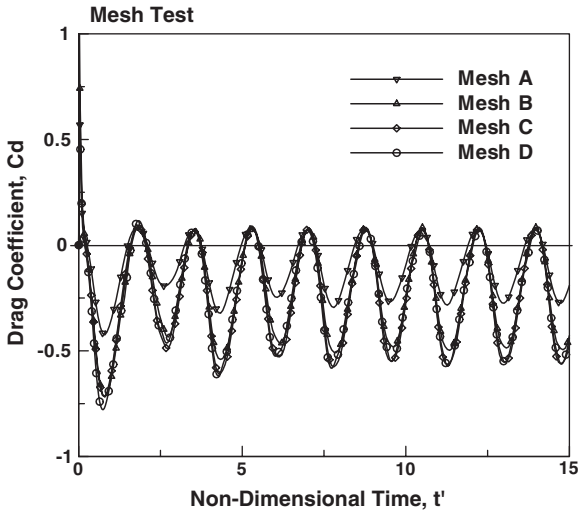

Fig. 5. Time variation of drag coefficient for four test grids.

Figs. 7(a) and (b) present the computed Mach number contours around the airfoil for the case where the airfoil is located at the central position of its plunge motion after four cyclic flapping motions. Note that Fig. 7(a) indicates the current results, while Fig. 7(b) presents those of Tuncer and Kaya (2003). As before, a good agreement is evident

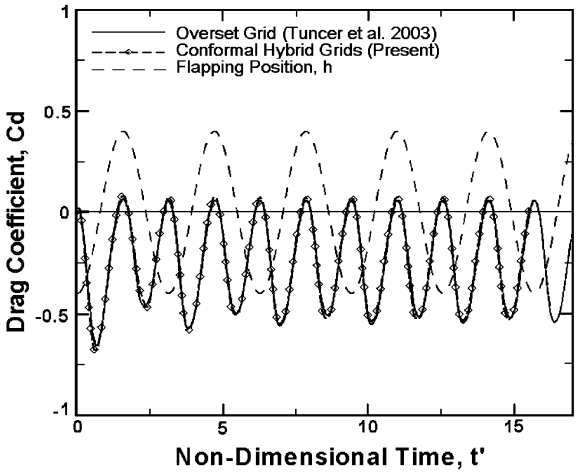

Fig. 6. Time variation of current drag coefficient computed at $k = 2$, $h_0 = 0.4$, $M = 0.1$ and $\mathrm{Re} = 10^4$ compared with results of Tuncer and Kaya (2003).

between the two sets of results. Furthermore, Fig. 7(a) confirms the ability of the present code to present very clearly the sizes and locations of the leading edge vortex and the vortex being shed from the trailing edge of the airfoil.

4. Results and discussion

The principal objective of the present study was to investigate the effect of the flexure amplitude on the aerodynamic propulsive efficiency and thrust of an NACA0014 airfoil during flapping motion. The starting premise of the study was that the computed aerodynamic performance would be strongly related to the deformation of the flexible airfoil as it executes cyclic dynamic plunge motion. As shown in Eq. (2), a quadratic equation based on the flexure amplitude, a_0, was employed to represent the shape of the flexible airfoil. As shown in Fig. 8, at each time step, the surface grids of the airfoil and the cells in the computational domain were reallocated by the dynamic mesh technique. This task was achieved by hooking a pre-written user defined function (UDF) program into the main code of the FLUENT solver during iterations.

The aerodynamic performance of a flexible flapping airfoil can be evaluated by means of two fundamental indexes, namely the magnitude of the thrust produced by the airfoil when in motion with various flexible flapping modes, and the input power, which is defined as the total consumptive work required generating the plunge and deflection motions of the airfoil. The propulsive power generated by the thrust force is considered to be useful power. In other words, achieving a large propulsive power serves no purpose if it is obtained at the expense of an increased flapping input power. The propulsive efficiency of an airfoil can be defined as the ratio of the propulsive power to the input power. This ratio provides a meaningful index when attempting to optimize the propulsive aerodynamic performance by considering airfoils of different flexure amplitudes.

Consider a flexible airfoil with chord length c, moving at a constant forward velocity, U_∞ , and performing a harmonic heave motion, $h(t)$, of amplitude h_0 and frequency ω, as shown in Fig. 3. If T denotes the period of oscillation, the period-averaged consumption power rate ($\bar{P}$) and the thrust force ($\bar{F}_x$) can be evaluated, respectively, as

$$\bar{P} = \frac{1}{T}\int_0^T F_n(t)\frac{\mathrm{d}S_n}{\mathrm{d}t}\,\mathrm{d}t,$$
$$\bar{F}_x = \frac{1}{T}\int_0^T F_x(t)\,\mathrm{d}t, \tag{3}$$

where $F_n(t)$ and $F_x(t)$ represent the instantaneous generated force components in the normal-direction and the x-direction of the airfoil surfaces, respectively. The term $\mathrm{d}S_n/\mathrm{d}t$ denotes the traveling velocity of the flexible airfoil as it executes the plunge motion.

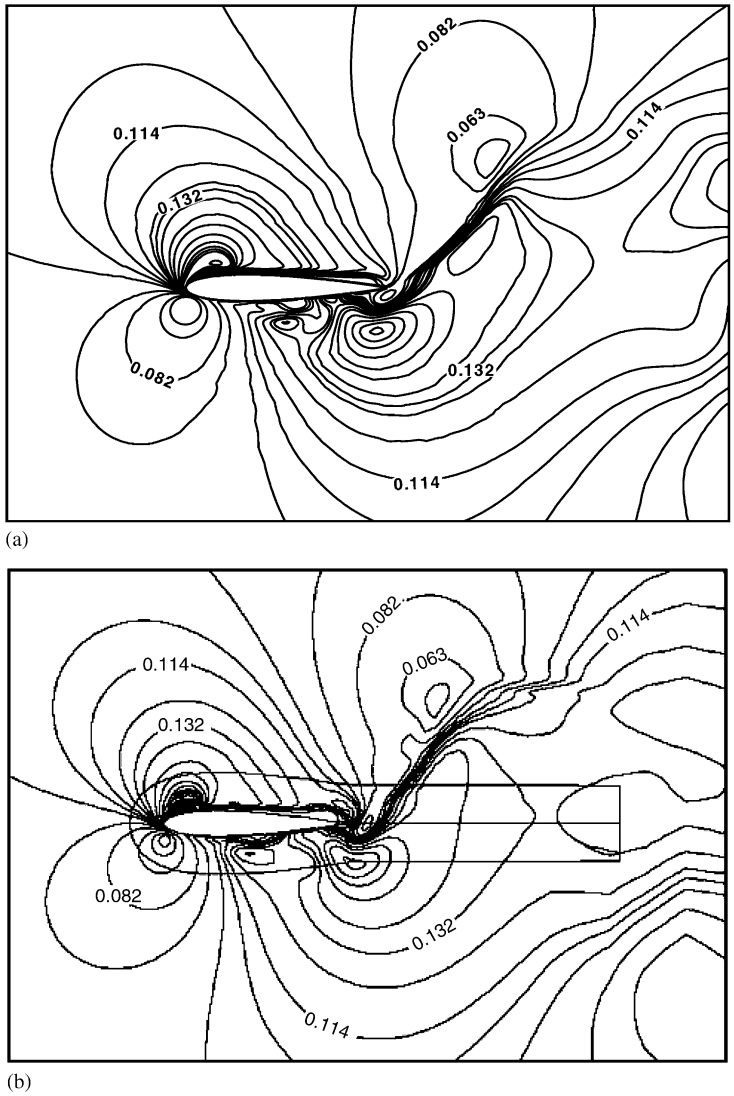

Fig. 7. Mach number contours computed at $k = 2$, $h_0 = 0.4$, $M = 0.1$ and $\mathrm{Re} = 10^4$ at middle position of stroke: (a) Computed by conformal dynamic hybrid-grids, present work; (b) Computed by overset grids, Tuncer and Kaya (2003).

The period-averaged consumption power rate is expressed in a nondimensional form and is defined as the period-averaged input power coefficient (δ), i.e.

$$\delta = \frac{\bar{P}}{(\frac{1}{2}\rho U_\infty^2 cs)U_\infty}. \tag{4}$$

The symbol ξ is defined as the period-averaged thrust power coefficient, and is expressed as

$$\xi = \frac{\bar{F}_x U_\infty}{(\frac{1}{2}\rho U_\infty^2 cs)U_\infty} = \frac{1}{T}\int_0^T (-C_d)\,\mathrm{d}t, \tag{5}$$

where ρ is the fluid density, s the span of the airfoil, and C_d the drag coefficient.

Therefore, the propulsive efficiency (η) can be defined as

$$\eta = \frac{\xi}{\delta}. \tag{6}$$

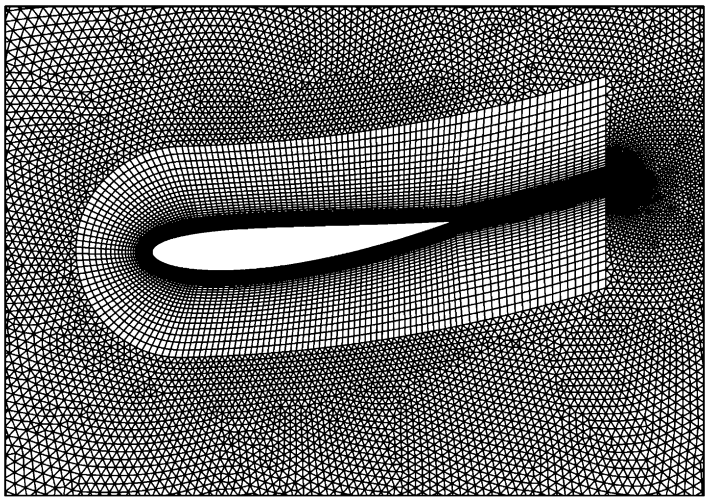

Fig. 8. Instantaneous grid distribution of flexible airfoil using dynamic mesh technology.

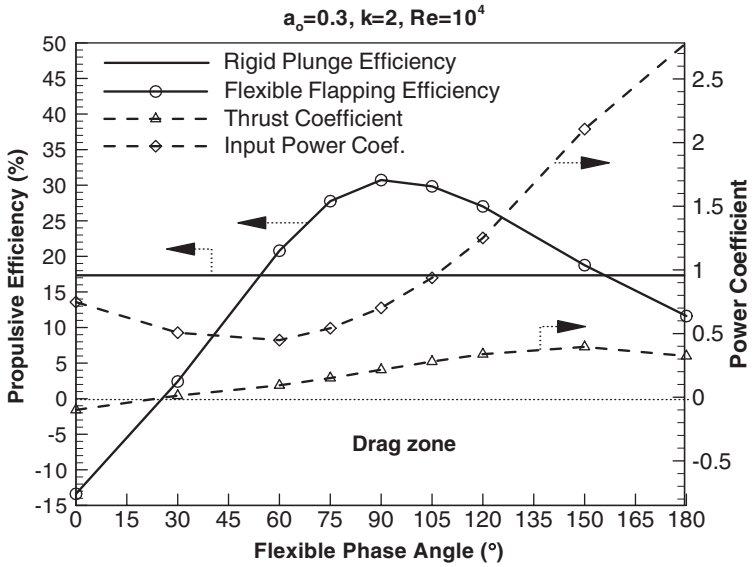

Fig. 9. Phase angle analysis for flexible flapping foil at $a_0 = 0.3$, $h_0 = 0.4$, $k = 2$ and $\mathrm{Re} = 10^4$.

Fig. 9 shows the variations of the input power coefficient (δ), the thrust power coefficient (ζ), and the propulsive efficiency (η) with respect to the phase angle between plunging and flexing for flow conditions of $\mathrm{Re} = 10^4$, $k = 2$, and $h_0 = 0.4$. Fig. 9 also displays that the maximum period-averaged thrust power coefficient occurs at $\psi = 150^{\circ}$, but the minimum input power coefficient occurs at $\psi = 60^{\circ}$. Compared with a rigid flapping airfoil, an enhancement in propulsive efficiency can be observed when the flexible airfoil with extent of 0.3 is flapping with appropriate phase angle at $60^{\circ} < \psi < 150^{\circ}$. In addition, the optimum phase angle is 90° for the flexible flapping airfoil to produce the maximum propulsive efficiency. Similar observations can be found in Read et al. (2003), Heathcote et al. (2004) and Heathcote and Gursul(2005). Therefore, the phase angle was fixed at 90° for all runs with respect to reduced frequency in this study.

In order to explore the effect of the flexure amplitude on the aerodynamic performance of the flapping airfoil, the present study specified values of $\mathrm{Re} = 10^4$, $k = 2$, and $h_0 = 0.4$, and computed the time variations of the drag coefficient

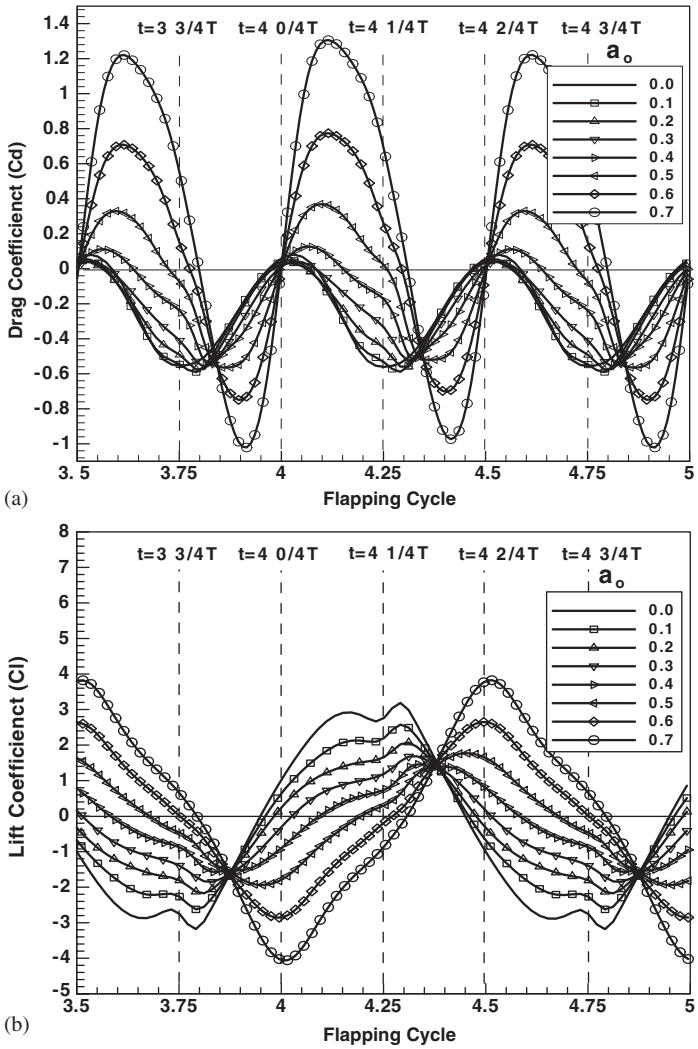

Fig. 10. Effect of flexure amplitude on time variation of C_d and C_l, computed at $k = 2$, $h_0 = 0.4$, $M = 0.1$ and $\mathrm{Re} = 10^4$: (a) Drag coefficient; (b) lift coefficient.

and the lift coefficient for eight different flexure amplitudes, a_0, ranging from 0 to 0.7 in intervals of 0.1. The corresponding results for the drag coefficient and the lift coefficient are presented in Figs. 10(a) and (b), respectively. In Eq. (5), a negative value of the drag coefficient indicates a positive thrust coefficient generated by the flapping airfoil. The results of Fig. 10 clearly demonstrate the key role played by the flexure amplitude in determining the aerodynamic coefficients of the flapping airfoil. Fig. 10(a) shows that the amplitude of the drag coefficient increases with increasing flexure amplitude. An examination of the results for the case of $a_0 = 0.7$ in the period $4\,T < t < 4.3\,T$ or $4.5\,T < t < 4.8\,T$ confirms that a high flexure amplitude yields a poor thrust coefficient performance. Moreover, the swept area of the high drag coefficient regions is enlarged and the location of the peak value delayed as the flexure amplitude increases. Compared to the rigid airfoil, i.e. $a_0 = 0$ (the solid line), the increase in thrust force obtained with an increasing flexure amplitude is evident only in the relatively narrow periods of $4.3\,T < t < 4.5\,T$ and $4.8\,T < t < 5\,T$. Fig. 10(b) plots the variation in the lift coefficient over time for different flexure amplitudes. It is observed that the lift coefficients of the rigid and flexible airfoils vary symmetrically to each other over time, i.e. when a positive lift force is generated for the rigid airfoil, a negative lift force is generated for the flexible airfoil, and vice versa. This leads to a variation of the total input power. For the rigid airfoil, it can be seen that a positive lift force is generated during the down stroke (i.e. $3.88T < t < 4.45T$), while a negative lift force is generated during the up stroke (i.e. $4.45T < t < 4.88T$).

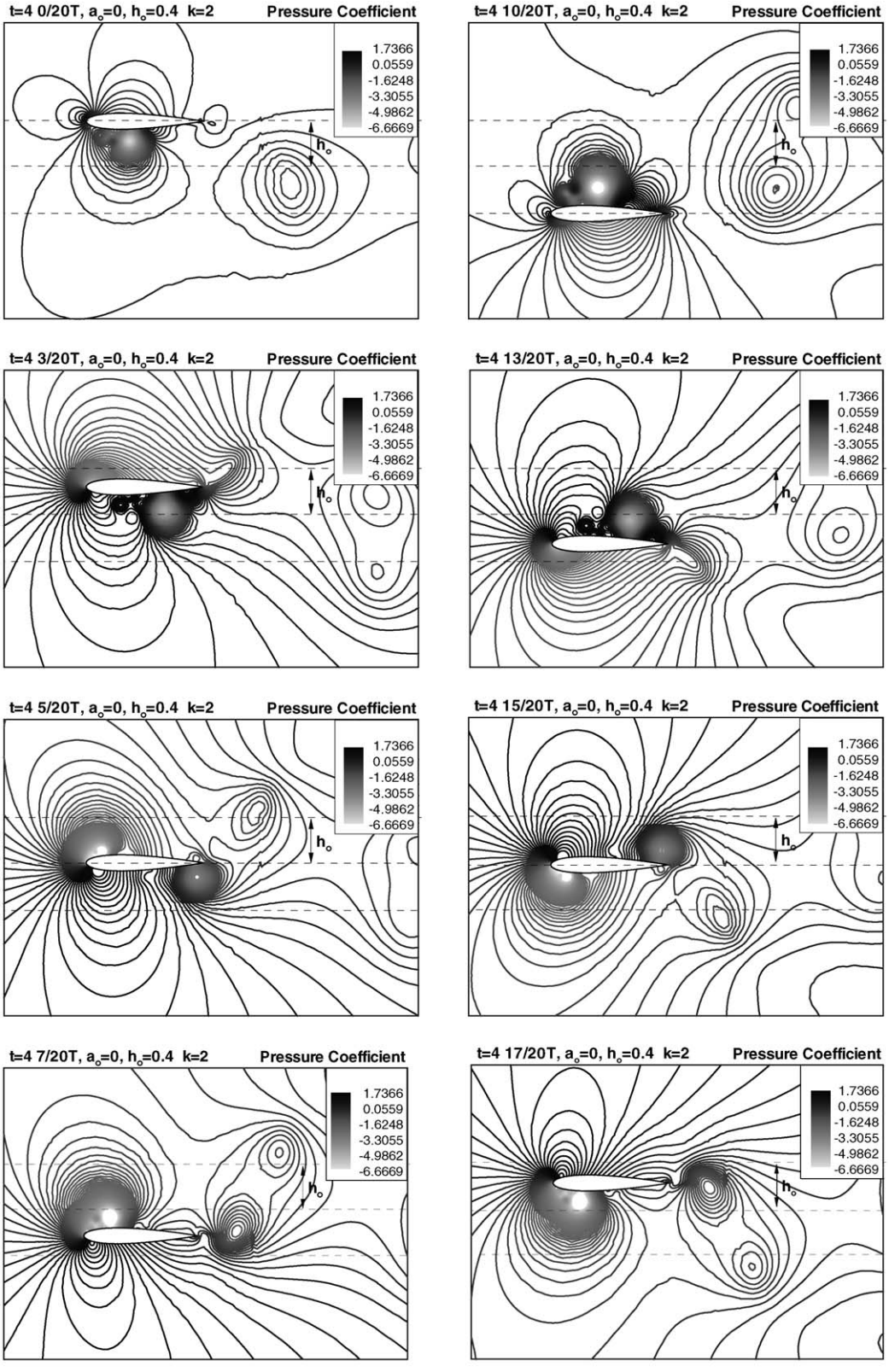

Fig. 11. Unsteady laminar flow over rigid flapping airfoil computed at $k = 2$, $h_0 = 0.4$, $\mathrm{Re} = 10^4$.

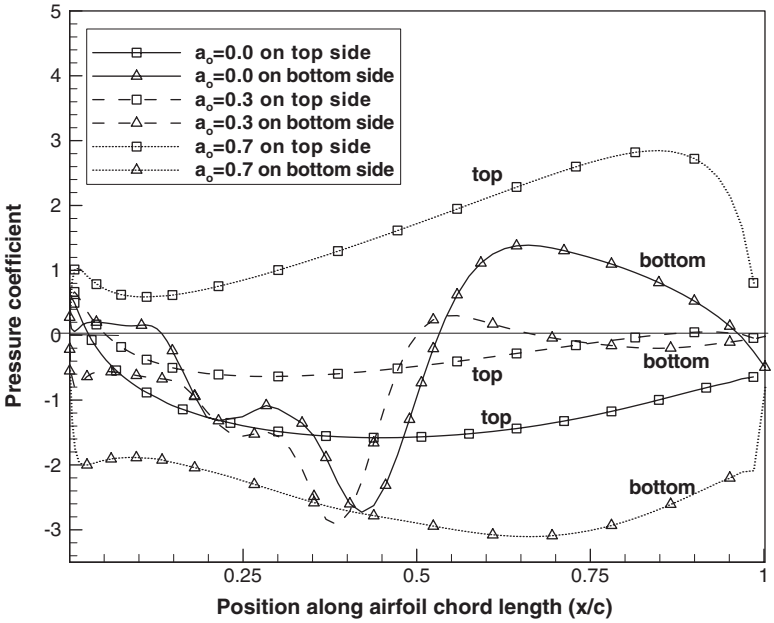

Fig. 12. Distributions of local static pressure coefficient on upper and lower surfaces of flapping airfoil at $t = (4+0/20)T$ for flexure amplitudes of $a_0 = 0$, 0.3, and 0.7.

Fig. 11 shows the evolution of the computed pressure coefficient contours around the rigid airfoil during one complete plunge motion cycle. Fig. 12 illustrates the variation of the local static pressure coefficient along the upper and lower surfaces of an airfoil with flexure amplitudes of 0.0, 0.3 and 0.7, respectively, at a time of $t = (4+0/20)T$. When the rigid airfoil is at its uppermost position at time $t = (4+0/20)T$, Fig. 11 shows that a low pressure core is located at the forward portion of the lower side. As shown in Fig. 10(b), the airfoil experiences a positive lift force at this point of the plunge cycle. This positive lift effect arises because the local static pressure on the upper surface of the airfoil is generally less than that on the lower surface.

Fig. 12 shows that for an airfoil with a flexure amplitude of $a_0 = 0$, a positive pressure coefficient exists on the rear portion of the lower surface of the airfoil. As the rigid airfoil travels toward the mid-point of the down stroke stage from $(4+0/20T)$ to $(4+5/20)T$, the low pressure core on the lower surface of the airfoil gradually moves toward the trailing edge, and a new low pressure core is formed on the top surface of the airfoil at the leading edge. The imbalances in the pressure distributions around the rigid airfoil result in either ascending or descending lift coefficients. As the rigid airfoil travels continuously toward its lowest position during the period $(4+5/20)T$ to $(4+10/20)T$, the lift coefficient gradually decreases as a result of the wake flow formed by the shedding of the low pressure core from the trailing edge of the airfoil. Meanwhile, the low pressure core on the upper surface of the airfoil moves gradually to a central position along the chord of the airfoil and then lifts off the surface, causing a relatively high pressure region to cover most of the aft portion. As the rigid flapping airfoil subsequently returns to its uppermost position over the period of $(4+10/20)T$ to $(5+0/20)T$, the pressure contours around the rigid flapping airfoil mirror the pattern observed in the preceding downward stroke.

When an airfoil with a higher flexure amplitude undergoes plunging motion in a free stream, it can be regarded as a continuously deforming elastic membrane. When the flexible airfoil is plunged in either the down-stroke or the up-stroke, the airfoil is shaped like a turbine rotor, as shown in Fig. 3. Fig. 12 clearly demonstrates the effect of the flexure amplitude in determining the nature of the local static pressure distributions along the airfoil at a time of $(4+0/20)T$. It can be seen that the pressure differential between the upper and lower surfaces of the airfoil increases as the flexure amplitude is increased. During the down-stroke stage, negative lift force coefficients are produced since the upper and lower portions of the flexible airfoil surfaces are analogous to the pressure and suction sides, respectively, of a turbine blade. As shown in Fig. 13, which illustrates the computed pressure coefficient contours around an airfoil with a flexure amplitude of $a_0 = 0.7$ over a complete plunge motion cycle, the relatively high pressure acting on the upper surface of the flexible airfoil induces negative lift force coefficients. Since the shape of the flexible airfoil is inverted during the up-stroke stage, the sign of the lift force coefficients are reversed during this stroke.

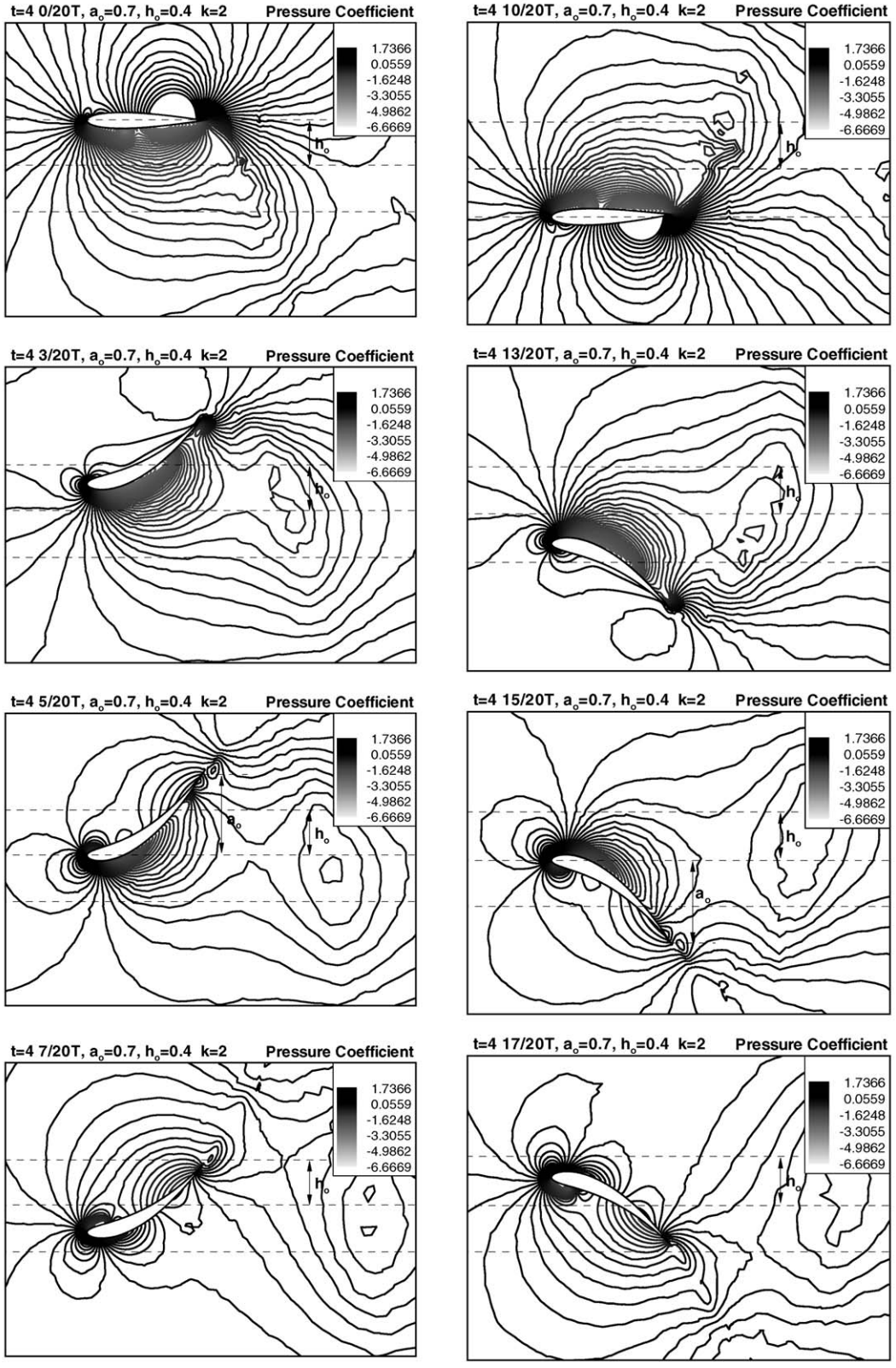

Fig. 13. Unsteady laminar flow over flapping airfoil with $a_0 = 0.7$ computed at $k = 2$, $h_0 = 0.4$, $\mathrm{Re} = 10^4$.

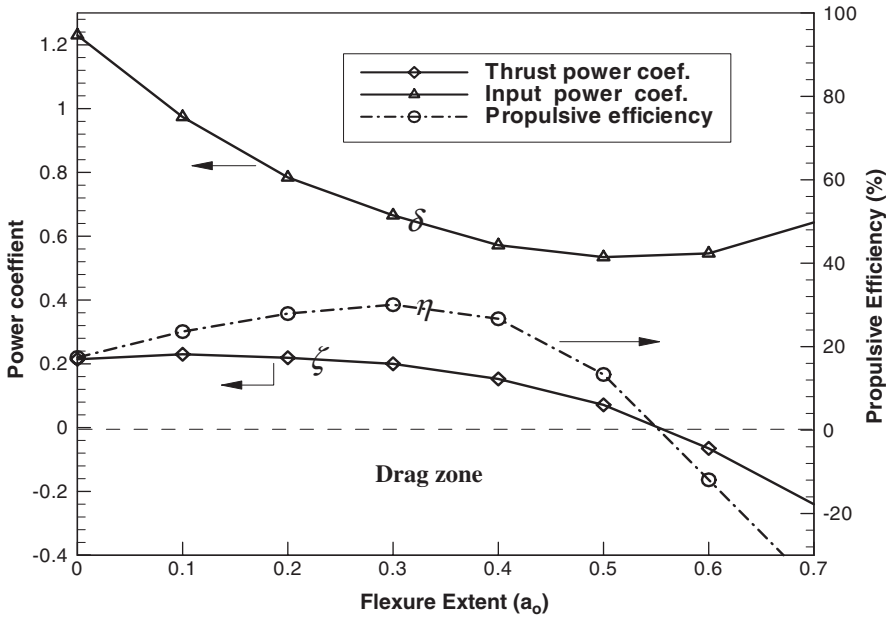

Fig. 14. Interrelationship between input power coefficient, thrust power coefficient and propulsive efficiency with respect to flexure amplitude computed at $k = 2$, $h_0 = 0.4$, $\mathrm{Re} = 10^4$.

Fig. 14 plots the variations of the input power coefficient (δ), the thrust power coefficient (ζ), and the propulsive efficiency (η) with respect to the flexure amplitude, a_0, for flow conditions of $\mathrm{Re} = 10^4$, $k = 2$, and $h_0 = 0.4$. In general, it is observed that the thrust power coefficient decreases with increasing flexure amplitude for $a_0 > 0.1$. Furthermore, it can be seen that the trend in the propulsive efficiency with increasing flexure amplitude is not monotonic. The propulsive efficiency initially increases by 100% as the airfoil is changed from rigid to flexible with a flexure amplitude of 0.3. The propulsive efficiency then decreases as the flexure amplitude is increased further. At flexure amplitudes of $a_0 = 0.6$ and 0.7, it is seen that the propulsive efficiency is less than zero since a drag force rather than a thrust force is produced as the flapping airfoil performs the plunge motion cycle.

Fig. 15 presents the evolution of the computed static pressure contours around a flapping airfoil with a flexure amplitude of $a_0 = 0.3$ over the course of one complete plunge cycle. Figs. 16(a) and (b) show the variation of the local pressure along the upper and lower surfaces of the airfoil, respectively, at various instants during the plunge cycle. Compared to the rigid airfoil considered in Fig. 11, it is apparent from Figs. 15 and 16 that the deformation of the airfoil with a flexure amplitude of 0.3 assists the vortex core in moving more smoothly from the leading edge to the trailing edge of the airfoil. Note that a similar characteristic is observed in dolphins, which beat their tails in the wake of their own bodies when swimming. In general, the observations of leading edge vortices moving chord-wise along the airfoil in the up-stroke and down-stroke of flapping motion means the occurrence of dynamic stall phenomena. The prediction of separation onset is an important issue for studies on the dynamic stall. To advance the understanding of the unsteady flows developed on rigid airfoil in flapping motion, considerable effort (Jones and Platzer, 1997; Jones et al., 2002; Lee and Basu, 1998) has been expended to investigate the flow structure by experimental and numerical approaches.

This study also investigated the effects of the Reynolds number and the reduced frequency on the aerodynamic performance of a flapping airfoil with a flexure amplitude of 0.3. Note that the nondimensional plunge amplitude was maintained at a constant of $h_0 = 0.4$ in all runs. Fig. 17 presents the variations of the period-averaged thrust power and input power coefficient with the reduced frequency for frequency values of $k = 1$–6 and Reynolds numbers of $\mathrm{Re} = 10^2$, 10^3 and 10^4, respectively. It can be seen that the reduced frequency value has a greater effect on the thrust power coefficients and input power coefficients than the Reynolds number. The thrust power coefficient increases linearly with the reduced frequency value in the tested range of Reynolds numbers. Tuncer and Kaya (2003) reported a similar trend for the variation of the thrust coefficient with the reduced frequency. It can be seen that the thrust power coefficient is greater at larger reduced frequencies and higher Reynolds numbers. This implies that a greater thrust force is generated

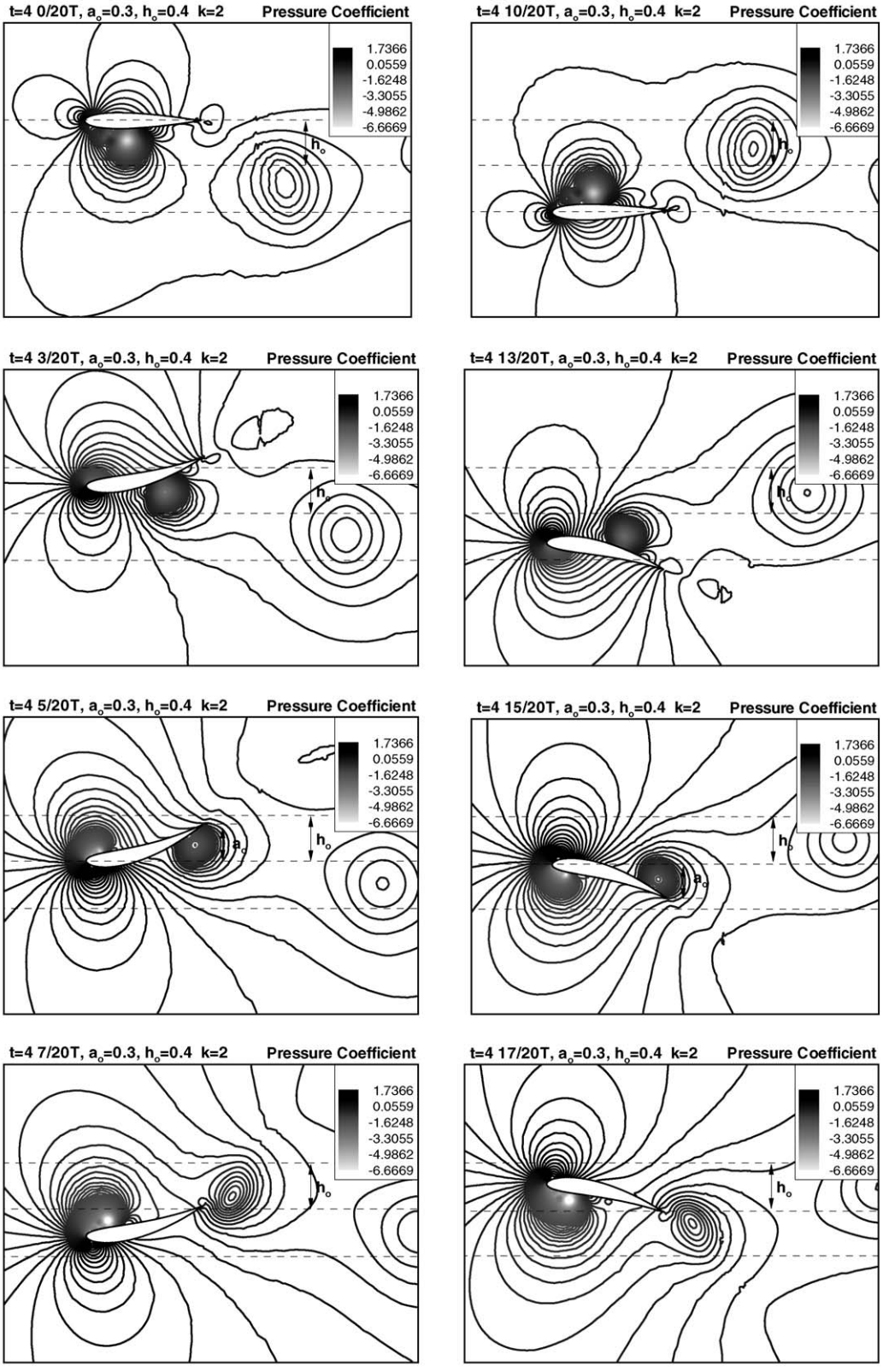

Fig. 15. Unsteady laminar flow over flapping airfoil with $a_0 = 0.3$ computed at $k = 2$, $h_0 = 0.4$, $\mathrm{Re} = 10^4$.

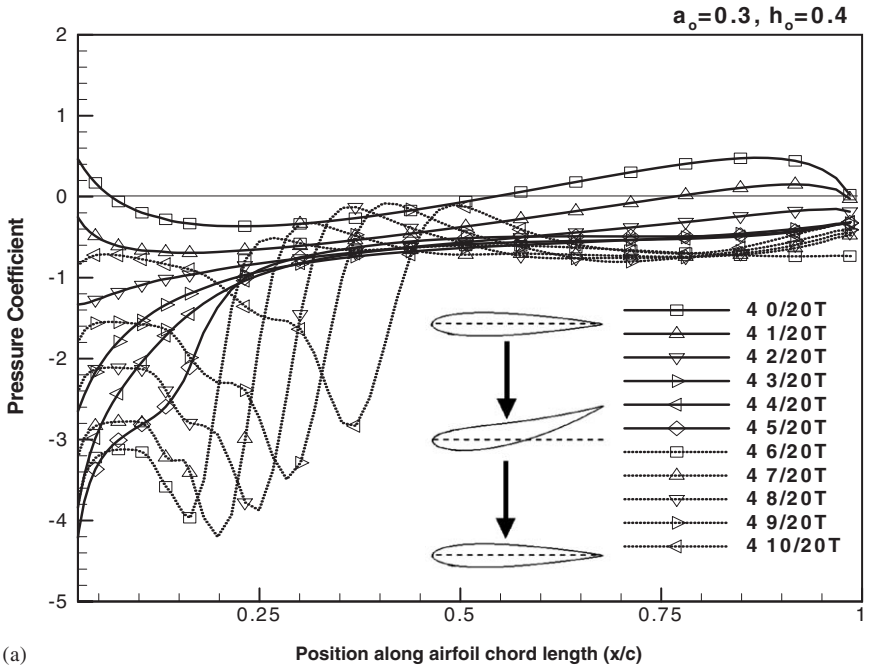

(a)

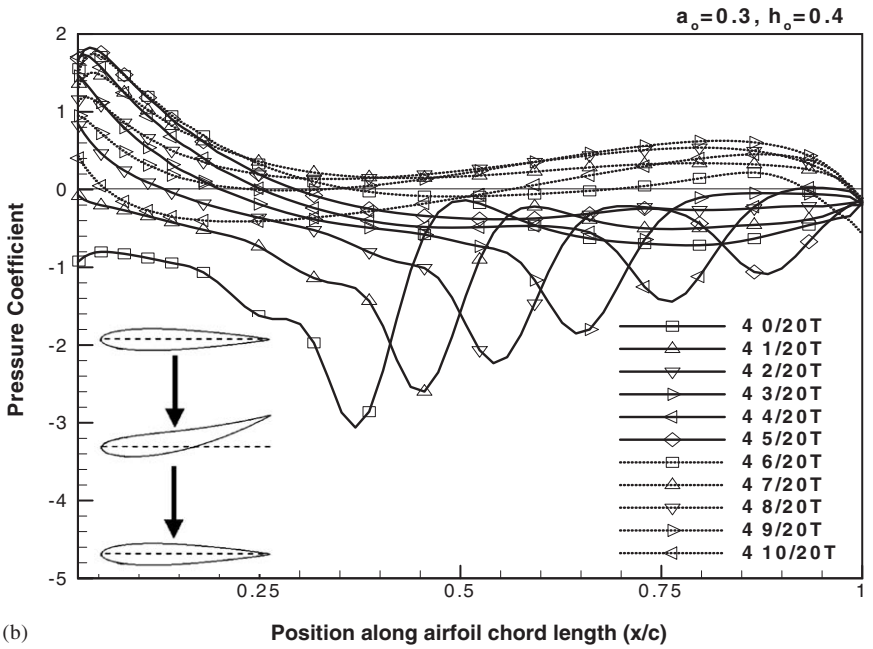

(b)

Fig. 16. Distributions of local pressure coefficient along upper and lower surfaces of flapping airfoil with $a_0 = 0.3$ at various time instants of plunge cycle: (a) upper surface; (b) lower surface.

at higher flapping frequencies. The input power coefficient increases exponentially as the reduced frequency increases. This trend can be attributed to the fact that a more rapid oscillation of the flexible airfoil in flapping motion requires the input of a greater mechanical power.

Fig. 18 illustrates the influence of the reduced frequency value on the propulsive efficiency of a flexible airfoil with a flexure amplitude of $a_0 = 0.3$ at Reynolds numbers of $\mathrm{Re} = 10^2$, 10^3 and 10^4, respectively. The overall domain is divided by the dashed line into an upper thrust-dominated zone and a lower drag-dominated zone. The reduced frequency

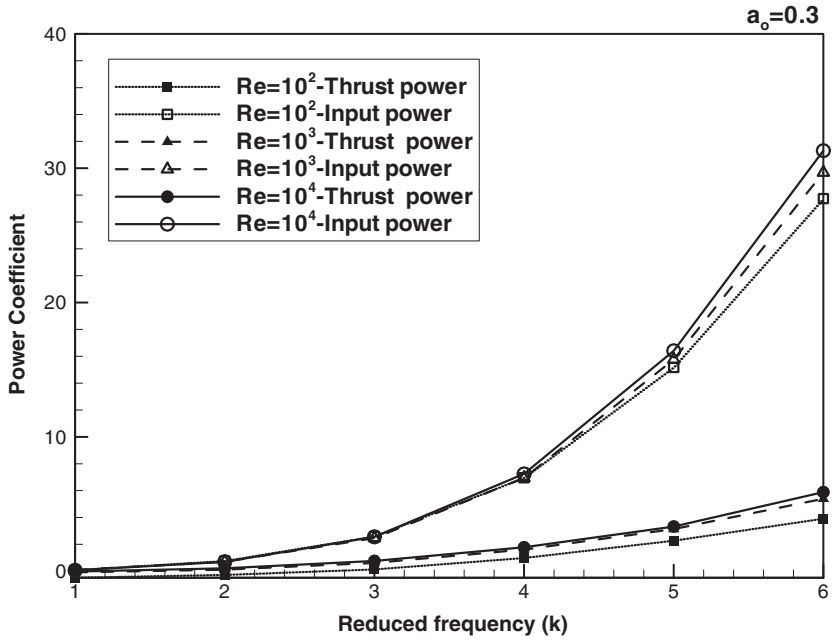

Fig. 17. Effect of reduced frequency on thrust power coefficient and input power coefficient at Reynolds numbers of $Re = 10^2$, 10^3, and 10^4.

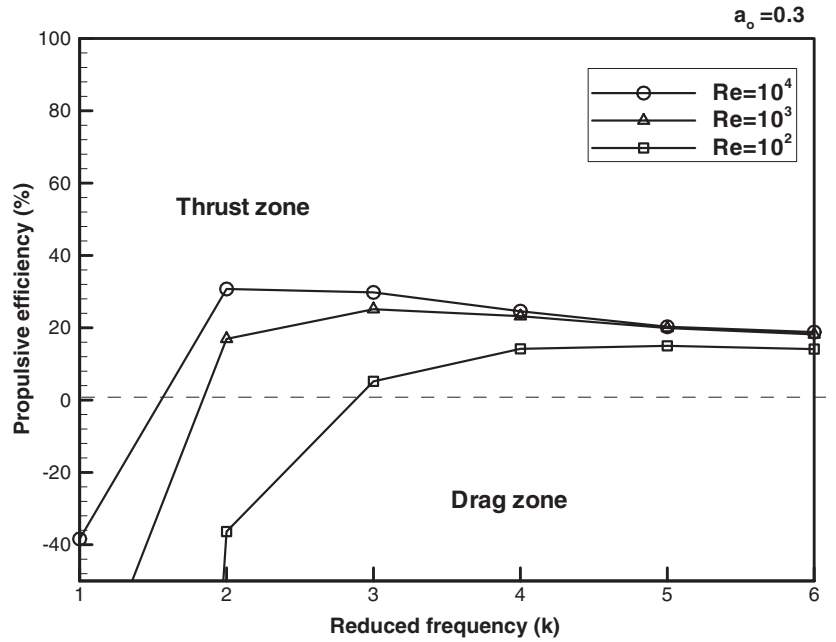

Fig. 18. Effect of reduced frequency on propulsive efficiency at Reynolds numbers of $Re = 10^2$, 10^3, and 10^4.

values corresponding to the peak propulsive efficiency at Reynolds numbers of $Re = 10^2$, 10^3 and 10^4 are found to be $k = 5$, 3, and 2, respectively. For a Reynolds number of 10^2, the flexible airfoil fails to produce a thrust force until the flapping reduced frequency has a value of $k = 3$. Fig. 18 shows that for a flexible airfoil, the enhancement in propulsive efficiency observed at higher Reynolds numbers is more pronounced at lower reduced frequencies. Of the various runs

performed in the present study, the airfoil with a flexure amplitude of 0.3 moving under conditions of $\mathrm{Re} = 10^4$, $k = 2$ and $h_0 = 0.4$, corresponding to a Strouhal number of approximately 0.255, demonstrates the highest propulsive efficiency, namely 30.73%.

5. Conclusion

An investigation of chord-wise flexible flapping-wing propulsion suitable for Micro Air Vehicles (MAVs) was accomplished. This study has employed Navier–Stokes analysis to compute the unsteady, viscous flow fields associated with low-Reynolds number flow over a single chord-wise flexible airfoil executing plunge motion. The computational domain has been constructed with conformal hybrid meshes and the dynamic mesh technique applied to illustrate the continuous deformation modes of the flexible flapping airfoil. To ensure a comprehensive examination of the influence of the flexure amplitude on the aerodynamic performance of the flapping airfoil at $\mathrm{Re} = 10^4$, $k = 2$, and $h_0 = 0.4$, the present study has considered eight flexure amplitudes, a_0, ranging from 0.0 to 0.7 in intervals of 0.1.

Thrust-indicative wake structures have been observed behind the trailing edge of the airfoil for airfoils with flexure amplitudes of 0.0–0.5 of the chord length. It has been shown that this wake structure evolves into a drag-indicative form as the flexure amplitude of the flapping airfoil is increased to 0.6 and 0.7 of the chord length. The results have shown that the propulsive efficiency is optimized when the flapping airfoil has a flexure amplitude of 0.3 of the chord length with phase angle of 90°. This study has also computed the propulsive efficiency and the propulsive thrust under various combinations of Reynolds number and reduced frequency. The numerical results have confirmed that the propulsive efficiency is influenced primarily by the value of the reduced frequency rather than by the Reynolds number. It has also been shown that the peak propulsive efficiency obtained at constant Reynolds numbers of 10^2, 10^3 and 10^4 occurs at reduced frequencies of 5, 3 and 2, respectively. Of the various runs performed in the present study, flow conditions corresponding to Strouhal number St of 0.255 are found to yield the highest propulsive efficiency of 30.73%. In order to achieve maximum propulsive efficiency, the present results also imply that the reduced frequency should be controlled to a small value for MAVs equipped with the chord-wise flapping wing with flexure extent of 0.3 flying in a flowstream of high Reynolds number.

References

Anderson, J.M., Streitlien, K., Barrett, D.S., Triantafyllou, M.S., 1998. Oscillating foils of high propulsive efficiency. Journal of Fluid Mechanics 360, 41–72.

Alexander, R.M., 1982. Locomotion of Animals. Chapman & Hall, Blackie, New York.

Betz, A., 1912. Ein beitrag zur erklärung des segelfluges. Zeitschrift für Flugtechnik und Motorluftschiffahrt 3, 269–272.

Hover, F.S., Haugsdal, Ø., Triantafyllou, M.S., 2004. Effect of angle of attack profiles in flapping foil propulsion. Journal of Fluids and Structures 19, 37–47.

Heathcote, S., Martin, D., Gursul, I., 2004. Flexible flapping airfoil propulsion at zero freestream velocity. AIAA Journal 42, 2196–2204.

Heathcote, S., Gursul, I., 2005. Flexible flapping airfoil propulsion at low Reynolds numbers. AIAA-2005-1405, Reno, Nevada, USA.

Isogai, K., Shinmoto, Y., Watanabe, Y., 1999. Effect of dynamic stall on propulsive efficiency and thrust of a flapping airfoil. AIAA Journal 37, 1145–1151.

Jones, K.D., Platzer, M.F., 1997. Method for the prediction of dynamic stall onset on turbomachinery blades. ASME Paper No. 97-GT-101, June.

Jones, K.D., Dohring, C.M., Platzer, M.F., 1998. An experimental and computational investigation of the Knoller–Betz effect. AIAA Journal 36, 1240–1246.

Jones, K.D., Castro B.M., Mahmoud O, Platzer M, 2002. Numerical and experimental investigation of flapping wing propulsion in ground effect. AIAA Paper 2002-0866, Reno, Nevada, USA.

Jones, K.D., Bradshaw, C.J., Papadopoulos, J., Platzer, M.F., 2004. Improved performance and control of flapping-wing propelled micro air vehicles. AIAA Paper No. 2004-0399, Reno, Nevada, USA.

Knoller, R., 1909. Die gesetze des luftwiderstands. Flug-und Motortechnik(Wien) 3, 1–7.

Lai, J.C.S., Platzer, M.F., 2001. The characteristics of a plunging airfoil at zero free-stream velocity. AIAA Journal 39, 531–534.

Lee, T., Basu, S., 1998. Measurement of unsteady boundary layer developed on an oscillating airfoil using multiple hot-film sensors. Experiments in Fluids 25, 108–117.

Murray, M.M., Howle, L.E., 2003. Spring stiffness influence on an oscillating propulsor. Journal of Fluids and Structures 17, 915–926.

Maxworthy, T., 1981. The fluid dynamics of insect flight. Annual Review of Fluid Mechanics 13, 329–350.

Read, D.A., Hover, F.S., Triantafyllou, M.S., 2003. Forces on oscillating foils for propulsion and maneuvering. Journal of Fluids and Structures 17, 163–183.

Rozhdestvensky, K.V., Ryzhov, V.A., 2003. Aerohydrodynamics of flapping-wing propulsors. Progress in Aerospace Sciences 39, 585–633.

Sitti, M., Campolo, D., Yan, J., Fearing, R.S., Su, T., Taylor, D., Sands, T.D., 2001. Development of PZT and PZN-PT based unimorph actuators for micromechanical flying mechanisms. IEEE International Conference on Robotics and Automation, Seoul, 3839–3846.

Tuncer, I.H., Kaya, M., 2003. Thrust generation caused by flapping airfoils in a biplane configuration. Journal of Aircraft 40, 509–515.

Tuncer, I.H., Platzer, M.F., 1996. Thrust generation due to airfoil flapping. AIAA Journal 34, 509–515.

von Kármán, T., Burgers, J.M., 1943. In: Durand W.F. (Eds.), General Aerodynamic Theory—Perfect Fluids. Vol. II of Aerodynamic Theory, Dover edition. Durand, p. 308.